PHYSICAL REVIEW C VOLUME 51, NUMBER 2 FEBRUARY 1995

High energy single particle states in the continuum

Angela Bonaccorso*
Istituto Nazionale di Fisica Nucleare, Sezione di Pisa, 56100 Pisa, Italy
and Institut de Physique Nucléaire, IN2P3-CNRS, 91406 Orsay, Cedex, France
(Received 24 August 1994; revised manuscript received 21 October 1994)

This paper contains new developments of the Bonaccorso-Brink reaction model for neutron transfer to continuum states in heavy-ion collisions. The spectral distributions, escape, and spreading widths of the neutron final continuum states are calculated and studied by introducing a semiclassical S matrix describing the rescattering of the neutron on the target. By comparing to previous calculations done with an optical model S matrix we suggest a method to estimate the damping of single particle states in the continuum. Our calculations for the transfer cross sections and for the single particle widths are compared to available experimental data. The results of the comparison support the interpretation of the structures in the experimental spectra up to an excitation energy as high as $E_x \sim 20$ MeV in ^{208}Pb and $E_x \sim 30$ MeV in ^{91}Zr as due to the population of single particle states of high spin.

PACS number(s): 25.70.Hi, 24.30.Gd

I. INTRODUCTION

One-neutron transfer to the continuum reactions have been used for many years to study the spectroscopy of low-lying single-particle resonance states in the continuum. Data taken up to 1988 were discussed in [1]. More recent data are published in [2–8, 10]. Many experiments have targets in the region of lead but also other nuclei as ^{48}Ca, ^{90}Zr, ^{120}Sn, and ^{64}Ni have been studied.

One characteristic common to almost all inclusive spectra is that there are structures up to an excitation energy of about $E_x \sim 10$ MeV. At higher excitation energies some spectra show a structureless continuum. This happens for light projectiles like α particles and/or when the incident energy is less than about $E_{\rm inc} = 30$ MeV/nucleon. However, there is a group of reactions in which the situation is rather different because the spectra show also structures at $E_x \sim$20–40 MeV superimposed to a large continuum. This happens in reactions in which both the projectile and the target are heavy ions and when the incident energy is of the order of $E_{\rm inc} \sim 40$ MeV/nucleon. This rather unexpected feature originated a number of speculations, namely, that the high-energy bump could be the signature of a giant collective resonance or it could simply represent the maximum of the physical background due to the breakup. Then in Ref. [9] it was shown that the transfer spectra were dominated by noncollective high-spin states. The calculations were done by describing the transfer within the distorted wave Born approximation and the collective states by the random phase approximation. On the other hand, in Ref. [10] it was shown that the background due to breakup could account only for about one-third of the cross section, the rest being due to neutron resonant absorption on the target. Some typical reactions showing high-energy structures are ^{207}Pb(^{20}Ne,^{19}Ne)^{208}Pb at $E_{\rm inc} =$ 48 MeV/nucleon [6, 10], and ^{208}Pb(^{40}Ar,^{39}Ar)^{209}Pb at $E_{\rm inc} = 41$ MeV/nucleon [6, 10], and ^{90}Zr(^{20}Ne,^{19}Ne)^{91}Zr at $E_{\rm inc} = 40$ MeV/nucleon [3].

Recently two new experiments have been performed to clarify the nature of both low-energy and high-energy structures. The reactions studied were ^{208}Pb(α,^{3}He)^{209}Pb at $E_{\rm inc} = 30$ MeV/nucleon [7] and ^{48}Ca(^{20}Ne,^{19}Ne)^{49}Ca at $E_{\rm inc} = 48$ MeV/nucleon [8]. In these experiments the neutrons emitted during the reaction have been detected at backward angles in coincidence with the ejectile in order to obtain information on the decay properties of the target resonance states populated by transfer. The analysis of the angular correlation in those data has shown that the reaction on ^{208}Pb is dominated by the absorption of the transferred neutron on the high-spin continuum states of the target, while the reaction on ^{48}Ca is dominated by the breakup. Furthermore, the inclusive spectrum of the ^{48}Ca(^{20}Ne,^{19}Ne)^{49}Ca reaction shows only a structureless continuum.

It is timely and appropriate to examine if such a rich variety of reactions having different combinations of projectile-target nuclei and incident energy, giving rise to inclusive spectra containing rather different proportions of transfer vs breakup components, can all be explained in the framework of the Bonaccorso-Brink model of tranfer to the continuum. Our previous interpretation of the inclusive experimental spectra [10–14] was dedicated to limited aspects of the physics contained in the nuclear reaction continuum and only recent developments of our model and the availability of exclusive measurements make this global review possible. The model treats indeed in a coherent way the processes of transfer to resonant states of the target [11], elastic breakup

---

*Present address: Institut de Physique Nucléaire, IN2P3 -CNRS, 91406 Orsay, Cedex, France.
Electronic address: Decnet 39186::BONAC
Internet: BONAC@THPISA.DIFI.UNIPI.IT

[12], and inelastic breakup [14]. Furthermore, numerical problems related to a proper use of the model have been carefully analyzed in Ref. [13], while preliminary comparisons with experimental data [10] have shown that the model is able to reproduce the main characteristics of the spectra.

One interesting aspect of the Bonaccorso-Brink model is that it allows decomposition of the cross section into the contributions of the various final angular momenta. Decomposition in terms of the final j_f is used explicitly in the present paper for the first time to study the single-particle properties of the continuum states populated by transfer. In fact each of these individual terms due to a final state of definite angular momentum is normalized by the transmission coefficient, Eq. (2.2) of the next section, describing absorption of the neutron on the target. Thus it contains the same physical information as the strength function or structure function of the state as defined in [1] and in [15], respectively.

In the present work we make new developments of the model which will allow us to extract, from the experimental spectra, information on the microscopic structure of the target resonant states populated in the reaction. The developments consist of the introduction of a semiclassical S matrix for the description of the neutron rescattering on the target. The semiclassical S matrix contains a Lorentzian shape for the resonance with an explicit dependence on the width. We will show that the decomposition of the width into a part due to direct decay and a part due to damping is a natural consequence of the semiclassical prescription. Then both the direct and spreading widths will be calculated. In particular, the spreading width will be calculated in three different ways because it gives the main contribution to the total width and we wanted to check the sensitivity of the results on the method used.

Finally the comparison with previous cross section calculations [10], where an optical model S matrix was used, will allow us to establish the origin of the structures in the experimental spectra as due to the population of single-particle states not only in the low-energy part of the spectra, but also at excitation energy $E_x \sim 20$ MeV in ^{208}Pb and $E_x \sim 30$ MeV in ^{91}Zr.

This paper is organized as it follows. In Sec. II, after a brief reminder of the basic formulas of the transfer to the continuum model, we introduce the semiclassical method to calculate the S matrix. The evaluation of the widths is discussed in Sec. III. Section IV contains a discussion of both the experimental and theoretical results and finally in Sec. V we give our conclusions.

II. SEMICLASSICAL S MATRIX

In the Bonaccorso-Brink model the neutron transfer probability from a definite single-particle state of energy ε_i, angular momentum l_i, and spin j_i in the projectile to a final continuum state of energy ε_f within an interval $d\varepsilon_f$ in the target is given by an incoherent sum of the transfer probabilities to each possible final j_f state in the energy bin $d\varepsilon_f$:

$$\begin{aligned}\frac{dP}{d\varepsilon_f} &= \sum_{j_f} \langle |1 - S_{j_f}|^2 \rangle B(j_f, j_i) \\ &= \sum_{j_f} (|1 - \langle S_{j_f} \rangle|^2 + T_{j_f}) B(j_f, j_i) \ , \end{aligned} \tag{2.1}$$

where

$$T_{j_f} = 1 - |\langle S_{j_f} \rangle|^2. \tag{2.2}$$

$\langle S_{j_f} \rangle$ is an energy averaged S matrix which describes the rescattering of the neutron on the target. The sum in Eq. (2.1) is over all possible final angular momenta corresponding to the given final energy. $B(j_f, j_i)$ is an elementary transfer probability which depends on the details of the initial and final states, on the energy of relative motion, and on the distance of closest approach between the two nuclei [11].

In Ref. [12] it was shown that the first term in Eq. (2.1), proportional to $|1 - \langle S_{j_f} \rangle|^2$, gives the elastic breakup spectrum while the second term proportional to the transmission coefficient T_{j_f} gives the absorption spectrum. The elastic breakup gives some part of the physical background of the spectra . The way of calculating it has been described in Refs. [13, 10]. The inelastic breakup comes from the absorption term from which it can be extracted according to the method described in Ref. [14]. It contributes also to the background.

In previous works and in some of the calculations shown in this paper the energy averaged S matrix appearing in Eq. (2.1) is calculated within the optical model with an energy-dependent optical potential. In this way we have been able to reproduce the experimental spectra to explain the structure of the bumps in terms of the individual j_f states contributing and also to estimate the resonance energy for each j_f state. On the other hand, as it will be shown in the following, the resonant behavior of the cross section for transfer to an individual j_f term might be due, in some cases, only to an optimum Q value effect. It is therefore important to establish a criterium to disentangle the single-particle properties of the final states from the resonant behavior of the cross section and in particular to check if the widths of the individual j_f terms appearing in Eq. (2.1) can give information on the single-particle state widths . To this purpose we start now to discuss the semiclassical S matrix.

Transfer to high-angular-momentum resonances is a peripheral process dominated by barrier penetration effects. These effects are important for potentials which are weakly absorbing at the barrier, the so-called surface transparent potentials. When the two nuclei are at the distance of closest approach there is an effective barrier between them such that the neutron can tunnel to a final continuum state in the target. Resonance states like the $1k_{17/2}$ in lead have positive energy, which is, however, below the barrier formed by the real plus centrifugal potential plus spin-orbit potential as shown in Fig. 1. In such a situation one can try to calculate the S matrix which appears in Eq. (2.1) by using a semiclassical approximation based on a WKB evaluation of the barrier penetration probability.

Some of the formulas used in the following are due to

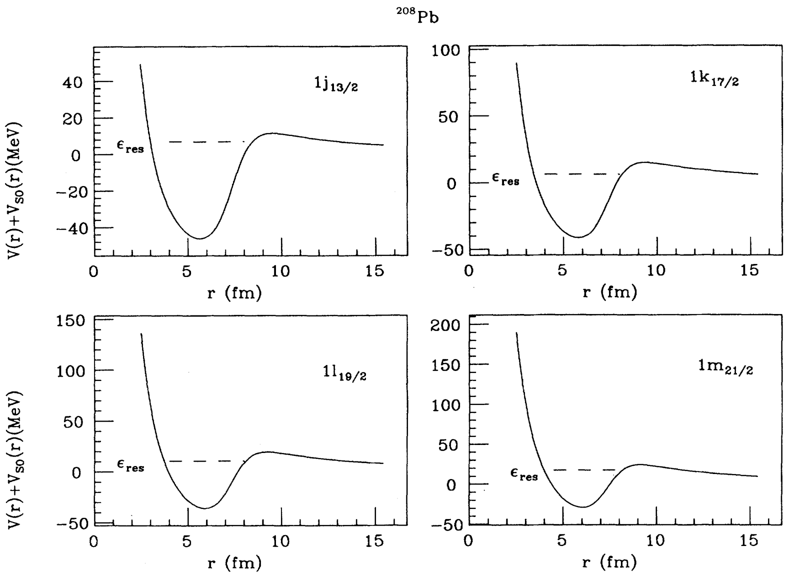

FIG. 1. Resonance particle states for ^{208}Pb in their respective potentials given by the sum of a Woods-Saxon plus spin-orbit term plus centrifugal potential.

Brink and Takigawa [16] and they are also discussed in Ref. [17]. The S matrix is given by

$$S = e^{2i\delta_1}\left[\frac{1+N\exp(2iS_{32})}{N+\exp(2iS_{32})}\right]. \tag{2.3}$$

The quantity δ_1 in Eq. (2.3) is the external phase shift which could be complex if there were direct reactions. We take it as zero since we are interested in discussing only the absorptive part of the scattering. Also

$$N^2 = 1+\exp(-2Q). \tag{2.4}$$

In Eq. (2.4) Q is a WKB barrier penetration integral and

$$P = 1-1/N^2 = \frac{1}{1+\exp(2Q)} \tag{2.5}$$

is a barrier penetration factor. The quantity S_{32} is defined in Appendix A. It is a WKB integral between turning points in the pocket behind the centrifugal barrier. It has a real part and an imaginary part corresponding to absorption, and so we can write

$$\exp(2iS_{32}) = A\exp(2i\psi)\ , \tag{2.6}$$

where A and ψ are real and $A < 1$.

We can get resonances by choosing $0 < A < 1$ and taking some suitable energy dependence for ψ. Then

$$1-|S|^2 = P\frac{1-A^2}{1+2A\sqrt{1-P}\cos(2\psi)+A^2(1-P)}. \tag{2.7}$$

One gets a resonance when $\cos(2\psi) = -1$. Expanding about the resonance position $\cos(2\psi) \approx -1+\alpha(\varepsilon_f-\varepsilon_{\rm res})^2$ gives

$$1-|S|^2 = P\frac{1-A^2}{(1-A\sqrt{1-P})^2}\frac{(\Gamma/2)^2}{(\varepsilon_f-\varepsilon_{\rm res})^2+(\Gamma/2)^2}. \tag{2.8}$$

A simple form for P would be to take a centrifugal barrier with a sharp cutoff at a radius R. We put $f = l(l+1)/(kR)^2$. Then

$$Q = kR\left[\sqrt{f}\ln\left(\sqrt{f}+\sqrt{f-1}\right)-\sqrt{f-1}\right] \tag{2.9}$$

if $f > 1$ (below the barrier) and $Q = 0$ if $f < 1$ (above the barrier), with the penetration factor given by $P = \exp(-2Q)$ which is appropriate for a sharp cutoff barrier.

A more accurate calculation of P would require the evaluation of the barrier penetration integral [17]

$$Q = \int_b^c |\gamma(r)|dr \tag{2.10}$$

at several energies around the resonance energy. This is not necessary for the calculation of Eq. (2.8) while it will be done for the calculation of the escape widths as we shall see in the next section. In Eq. (2.10) b and c are the outer and outermost turning points and

$$\gamma^2(r) = \left|\frac{2m}{\hbar^2}(V(r)-\varepsilon_{\rm res})+\frac{l(l+1)}{r^2}\right|\ , \tag{2.11}$$

where $V(r)$ is the sum of the real plus spin-orbit potential.

III. WIDTH

A. Escape width

In Eq. (2.8) Γ is the total width of the resonance. In Appendix A we show that it is approximately given by [17,18]

$$\Gamma \approx \Gamma_0+\Gamma^{\downarrow}\ , \tag{3.1}$$

where

$$\Gamma_0 = \hbar P/T \tag{3.2}$$

is the escape width which is due to the decay of the resonance by barrier penetration and

$$\Gamma^{\downarrow} \sim 2\langle W \rangle \tag{3.3}$$

is the spreading width defined in terms of the expectation value of the imaginary potential. The spreading width and the definition of $\langle W \rangle$ will be discussed in the next section.

In Eq. (3.2) P is the barrier penetration factor discussed in the previous section and T is the period of the radial motion of the particle in the real potential pocket inside the barrier [19]

$$T = \frac{2m}{\hbar^2}\int_a^b \frac{1}{|\gamma(r)|}dr \ , \tag{3.4}$$

where a is the internal turning point.

Equation (3.1) corresponds to the usual definition of the single-particle width as the sum of an escape width and a spreading width. However, one has to keep in mind that this distinction is somehow arbitrary because the direct decay of the particle which is represented by the escape width is modified by the coupling to other modes of excitation of the nucleus which are described by the spreading width. Therefore the evaluation of the escape width is very sensitive to the model used.

The definition of the escape width given in Eq. (3.2) takes into account only the interaction of the particle with a static potential. The quasiparticle-phonon model used instead in Ref. [20] treats the single-particle potential as a dynamic quantity calculated within the random phase approximation and we expect that the escape widths calculated in this way would be larger than ours.

The interesting point about Eq. (3.2) is that although it is very easy to calculate it gives results quite accurate, comparable to those obtained in Ref. [20] and in Ref. [21]. However, it is important to notice that in all methods the values of the escape width depend very much on the parameters used to define the single-particle potential. Our method is mainly sensitive to the value of the radius parameter which determines the position of the top of the barrier. Small changes in the potential give rise to changes in the turning points in Eqs. (2.10) and (3.4) and the overall effect can be a variation of a factor 2 or more on the value of the escape width. Then the agreement between various methods refers only to the order of magnitude.

Another advantage of Eq. (3.2) is that it can be used to estimate the escape widths of states of very high angular momentum like the $1l_{19/2}$ and $1m_{21/2}$ in lead which are interesting for the present discussion and which could not be studied with the methods of [20, 21]. Also it allows one to understand the variation of the escape width with the resonance energy. To discuss this point we show in Fig. 1 for ^{208}Pb, the real plus centrifugal plus spin orbit potentials relative to $l_f = 7$, $l_f = 8$, $l_f = 9$, and $l_f = 10$, respectively. The resonance energies indicated correspond to the peaks of the l terms shown in Fig. 4 and they are given also in Table III.

It is easy to understand that by increasing the resonance energies the barrier penetration range decreases, thus giving a larger barrier penetration factor P. At the same time the period increases because the particle makes a wider orbit inside the potential. But while the variations of P are of an order of magnitude in the case of $l_f = 7$ and $l_f = 8$, the variations of T are only few percent; therefore the escape width increases by raising the resonance energy for a given l_f state. This discussion is illustrated by the values of Γ_0, P, and T given in Table I for ^{208}Pb. P was calculated from Eqs. (2.5) and (2.10) and T from Eq. (3.4). The possible values of the resonance energies given in Table I for each l_f state are taken around the values given in Table III and they are all below the top of their respective potential barriers as shown in Fig. 1.

The interesting point is that while low-lying resonances like $1k_{17/2}$ have very small escape widths, other states of higher angular momentum and higher resonance energy have larger escape widths although they still maintain quite strong single-particle characteristics as we shall see

TABLE I. Escape and spreading widths from Eqs. (3.2) and (3.5) in ^{208}Pb.

l_f	$\varepsilon_{\rm res}$ (MeV)	P	T (10^{-22} sec)	Γ_0 (MeV)	$\Gamma^{\downarrow}$ (MeV)
7	3	0.10×10^{-3}	1.67	0.44×10^{-3}	3.36
7	5	0.38×10^{-2}	1.74	0.15×10^{-1}	4.15
7	7	0.35×10^{-1}	1.91	0.12	5.04
7	9	0.15	1.96	0.50	5.49
8	4	0.30×10^{-4}	1.46	0.13×10^{-3}	3.88
8	6	0.78×10^{-3}	1.54	0.30×10^{-2}	4.75
8	8	0.71×10^{-2}	1.63	0.28×10^{-1}	5.42
8	10	0.36×10^{-1}	1.68	0.14	6.09
9	14	0.05	1.51	0.20	6.99
9	16	0.13	1.69	0.49	7.29
9	18	0.27	1.79	0.97	7.51
9	20	0.45	2.20	1.34	7.36
10	18	0.04	1.34	0.19	8.53
10	20	0.09	1.41	0.45	8.39
10	22	0.20	1.55	0.86	8.75
10	24	0.35	1.72	1.35	8.69

in the following sections.

The calculations in this section have been done by using MATHEMATICA [22].

B. Spreading width

The second term in Eq. (3.1) corresponds to the spreading width. We have defined it in terms of the average imaginary potential inside the barrier to be consistent with the discussion in Sec. II where we described the neutron target interaction by an optical potential. However, it is important to point out that Eq. (3.3) is quite generic and that there is not a unique prescription for calculating $\langle W \rangle$. In Appendix A we derive Eq. (3.1) within the semiclassical approximation to the S matrix and we show that in order to be consistent with the approximation, the spreading width has to be defined as the time average of the imaginary potential

$$\Gamma^{\downarrow} = -2\frac{\int_a^b W(r(t))dt}{\tau}. \tag{3.5}$$

Another possible definition of the average potential giving the spreading width can be obtained in the framework of the nuclear many-body theory [23]. In that approach the spreading width, also called the damping width, is related to the imaginary part of the self-energy which appears in the definition of the Green function of an excitation [15, 23]. The definition given in Ref. [23] is the following:

$$\Gamma^{\downarrow} = -2\int \rho(r)W(r)\; d^3r \;, \tag{3.6}$$

where $\rho(r)$ is the single-particle density given by $\rho(r) = |\psi(r)|^2$ and $\psi(r)$ is the single-particle wave function. In Appendix B it is shown that if one uses for $\psi(r)$ the semiclassical form of the wave function, then Eq. (3.5) and Eq. (3.6) are equivalent.

There are two important characteristics of the spreading widths that we wish to study, namely, their dependence on the energy and on the angular momentum. Equation (3.5) depends on the angular momentum in several ways. One is that the classical orbit along which we are taking the time integral of W is in fact angular momentum dependent. We should have written $r_\lambda(t)$ where $\lambda = l + 1/2$ is the classical angular momentum corresponding to the quantum angular momentum l. Then the angular momentum enters also in the centrifugal potential and as a consequence the period of the classical orbit inside the real potential pocket and the turning points will depend on l. The energy dependence of $\Gamma^{\downarrow}$ is due mainly to the fact that the strength of W is energy dependent and also to the dependence of the period and of the turning points on the resonance energy.

On the other hand, Eq. (3.6) depends on the angular momentum because of the dependence on the single-particle wave function $\psi_{lm}(r)$ and on the energy because both ψ and W are energy dependent. However, in Ref. [23] it was argued that the density of single-particle orbitals $\rho(r)$ which appears in Eq. (3.6) could be taken to be constant in the vicinity of the absorptive region. This assumption is justified by the fact that the imaginary potential varies appreciably only on the surface of the nucleus where the radial parts of the wave functions of the high-spin single-particle states that we are studying in this paper are also peaked. Then according to Ref. [23] one can write

$$\Gamma^{\downarrow}(\varepsilon_f) = 8\pi\, \tilde{\rho} \int r^2 dr\; W(r, \varepsilon_f) \;, \tag{3.7}$$

where $\tilde{\rho} \sim 0.08$ fm$^{-3}/A$ is an average density of the single-particle orbitals in the vicinity of the absorptive region. The value chosen is half the nuclear matter density. This approximation allows us to use the Brown-Rho [24] parametrization for the volume integral of the optical potential which appears in Eq. (3.7)

$$[r^2]_W^{BR} = \frac{4\pi}{A}\int r^2 dr\; W(r,\varepsilon_f) = -b_2\frac{(\varepsilon_f - E_F)^2}{(\varepsilon_f - E_F)^2 + r_2^2} \;. \tag{3.8}$$

According to Mahaux and Sartor [25] the values of the parameters in Eq. (3.8) for the neutron-^{208}Pb potential are $b_2 = 70.95$ MeV fm^3, $r_2 = 10.87$ MeV, and $E_F = -5.65$ MeV. In Ref. [25] it was shown that the energy dependence of the volume and surface strengths of the imaginary potential saturates around 40 MeV, then according to Eq. (3.7) the widths $\Gamma^{\downarrow}(\varepsilon_f)$ are constant for energies in a continuum larger than 40 MeV and the single-particle effects disappear. The widths obtained from Eqs. (3.7) and (3.6) are given in Table II(a). Our values are in agreement with those given in Refs. [1, 23].

Furthermore, in Table I we give, for several angular momenta and energies, the spreading widths obtained from Eq. (3.5). It is interesting to notice that there is some dependence on the energy for each fixed angular momentum but there is not much dependence on the angular momentum for a fixed energy. However, there is a continuous smooth increase of the width increasing the energy, and the widths obtained with this method agree within 20% with the widths of Table II(a). One could get a better agreement just by choosing a slightly different value of the constant density of orbitals in Eq. (3.7).

TABLE II. (a) Spreading width as a function of the continuum energy in ^{208}Pb. (b) Spreading width as a function of the continuum energy in ^{91}Zr. All units are in MeV.

(a)								(b)	
ε_f	$\Gamma^{\downarrow}$	ε_f	$\Gamma^{\downarrow}$	ε_f	$\Gamma^{\downarrow}$	ε_f	$\Gamma^{\downarrow}$	ε_f	$\Gamma^{\downarrow}$
1	3.1	11	7.9	21	9.7	31	10.4	1	9.7
2	3.7	12	8.2	22	9.8	32	10.5	5	10.14
3	4.4	13	8.5	23	9.9	33	10.5	10	10.67
4	5.0	14	8.7	24	10.0	34	10.6	15	11.21
5	5.5	15	8.9	25	10.1	35	10.6	20	11.74
6	6.1	16	9.1	26	10.2	36	10.6	25	12.28
7	6.5	17	9.2	27	10.2	37	10.7	30	12.81
8	6.9	18	9.3	28	10.3	38	10.7	35	13.35
9	7.3	19	9.5	29	10.3	39	10.7	40	13.88
10	7.6	20	9.6	30	10.4	40	10.7		

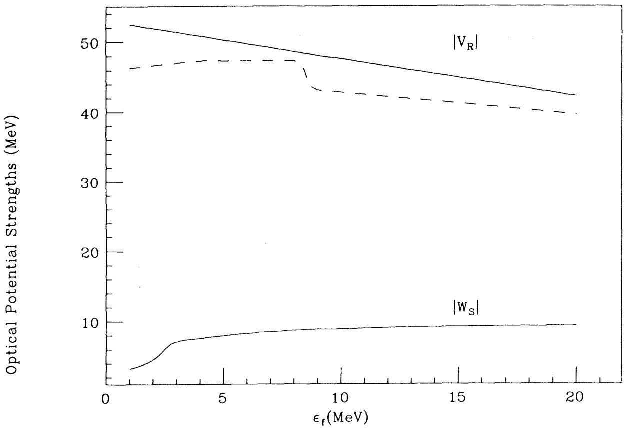

FIG. 2. Energy parametrization of the optical potential strengths for ^{120}Sn (solid curves) and ^{64}Ni (dashed curve).

The choice of the most appropriate $\tilde{\rho}$ is discussed in Appendix C where we show the radial dependence of the imaginary potential and of the radial wave functions of some high-spin resonance states which have been calculated numerically. With those wave functions it is possible to calculate Eq. (3.6) exactly and to compare the spreading widths obtained in this way to those obtained using the approximation of a constant density of orbitals.

The reason why we wish to study in detail the validity of Eq. (3.6) is that together with Eqs. (3.7) and (3.8) it gives a very simple way of estimating the spreading widths by relating them to the parametrizations of the imaginary potential. The calculation of Eq. (3.5) requires instead the numerical calculation of the turning points, of the period of the radial motion, of the classical trajectory of the particle within the real potential, and finally of the time integral of the imaginary potential.

IV. RESULTS AND DISCUSSION

In this section we discuss the results of the calculations made for the reactions mentioned in the Introduction and we compare them to the corresponding experimental spectra. We start by giving some information on the optical potential parametrizations used in this paper.

To get the energy dependence of the strength of the imaginary part of the neutron-^{208}Pb optical potential we followed two different parametrizations given by Mahaux and Sartor [15, 25]. We have found that the parametrization of Ref. [25] gives a good description of the high-energy part of the spectra and we have used it for the calculations relative to the reaction ^{207}Pb(^{20}Ne,^{19}Ne)^{208}Pb at $E_{\text{inc}} = 48$ MeV/nucleon together with the real potential of Ref. [10] while we have used both the real and imaginary potential of [15] with a spin-orbit strength $V_{\text{s.o.}} = 7$ MeV for the reaction ^{208}Pb(α,^{3}He)^{209}Pb at $E_{\text{inc}} = 30$ MeV/nucleon because it gives a better description of the spectra at low excitation energy.

For the reactions having ^{48}Ca and ^{90}Zr as a target we used the parametrizations suggested in [15] and [26] respectively. For the other two targets ^{120}Sn and ^{64}Ni we have constructed our own parametrization since there is none in the literature. In both cases we used an optical potential having only a surface imaginary part. In Fig. 2 the solid lines show the strengths of the real and imaginary parts used for ^{120}Sn while the dashed line shows the real potential strength used for ^{64}Ni. The imaginary part parametrization was the same as that suggested in [15], corrected for the appropriate Fermi energy which we took to be equal to $E_F = -8$ MeV.

First we discuss the group of reactions made at $E_{\text{inc}} =$ 30 MeV/nucleon and having the α particle as a projectile. These reactions are easier to analyze because there is only one initial state in the projectile to be taken into account. For a discussion of the initial state effect we refer the reader to Refs. [10] and [13].

Figure 3(a) shows the experimental and calculated spectra of the reaction ^{208}Pb(α,^{3}He)^{209}Pb at $E_{\text{inc}} = 30$ MeV/nucleon. The solid curve (a) is the calculated inclusive cross section which is arbitrarily normalized to the experimental spectrum from [7] while the solid curve (b) is the breakup part of the spectrum multiplied by a factor of 10. We give also the energy distribution of the cross section corresponding to the absorption term in Eq. (2.1) for some fixed values of the final angular momentum, namely, $l_f = 6 - 10$. For each l_f the contributions corresponding to $j_f = l_f \pm 1/2$ were summed. This is possible because the transfer probability, Eq. (2.1), contains an incoherent sum of final j_f values. We remind the reader that for this calculation we have used the optical potential of Ref. [15].

In Fig. 3(b) we show again some of the calculations of Fig. 3(a) made with the optical model S matrix (solid curves) while the dotted curves were obtained using the semiclassical S matrix, Eq. (2.8), discussed in Sec. II. The width appearing in Eq. (2.8) is the total width but from the values of the escape and spreading widths given in Tables I and II(a), respectively, we see that the escape widths are negligible compared to the spreading widths and therefore we shall use Eq. (2.8) with $\Gamma \approx \Gamma^{\downarrow}$. We have used Eq. (2.8) with A=0.93 for $l_f = 8$, A=0.9 for $l_f = 9$, and A=0.85 for $l_f = 10$. The parameter A gives the magnitude of the S matrix. Values of A close to 1 are appropriate for a weak absorptive potential. The values of $\Gamma^{\downarrow}$ are given in Table II and were obtained from Eqs. (3.7) and (3.8). The resonance energies in Eq. (2.8) were taken as the peak energies of the l_f-resonant terms obtained from the optical model calculation.

In Fig. 3(b) we notice that the absolute values of the cross sections calculated with the two different methods agree in all cases. This proves that the semiclassical S matrix is a good approximation to the optical model S matrix for the kind of reactions we are concerned with in this paper. According to Eq. (2.8) the single-particle resonance states have a Lorentzian energy distribution around the resonance energy. By looking at Fig. 3(a) we notice that for the $l_f = 8$, $l_f = 9$, and $l_f = 10$ resonances also the optical model calculation gives an energy distribution very close to a Lorentzian. Therefore in all cases the Lorentzian approximation to the spectral distribution of the single-particle states in the continuum seems to be correct. Also the values of the widths obtained from Eq. (3.7) agree with the exact values implicitly contained in the optical model S matrix and we can say that Eq. (3.7)

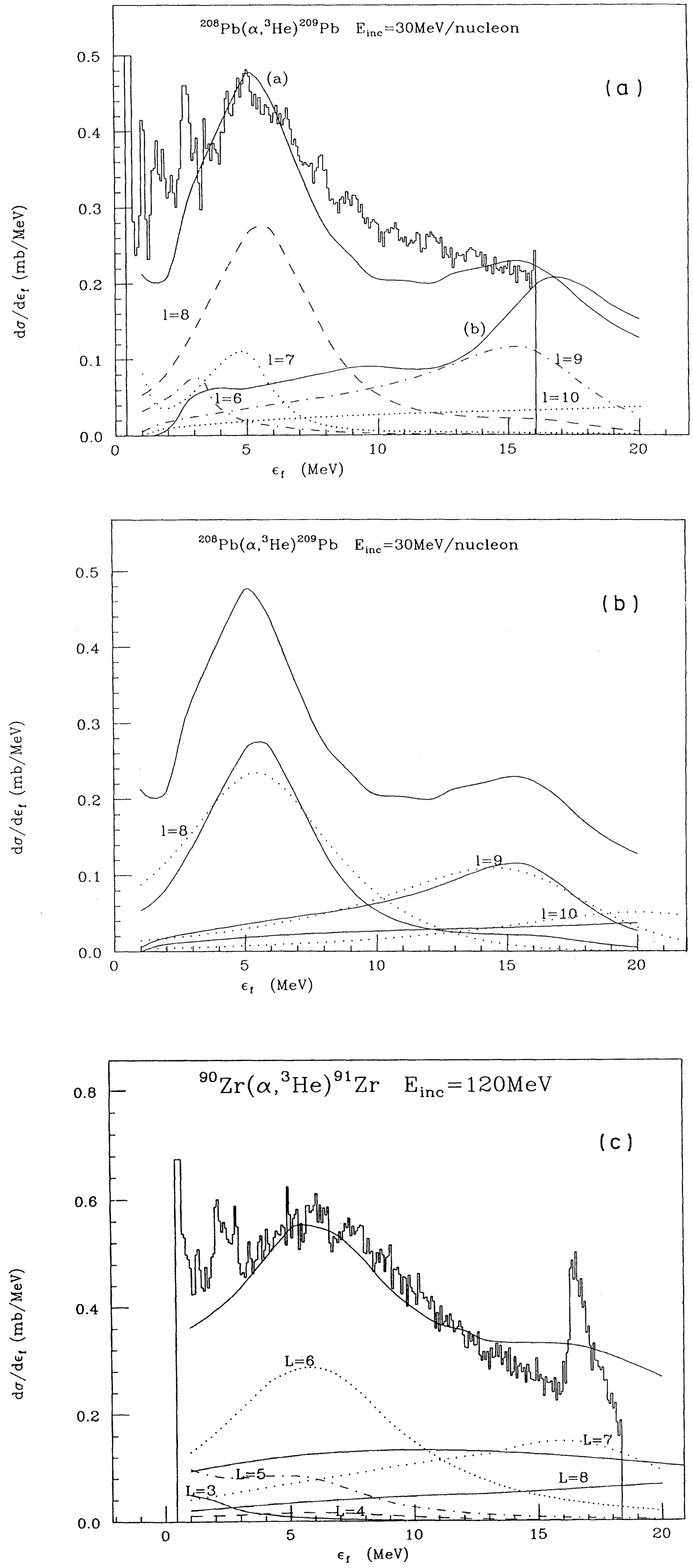

FIG. 3. (a) Inclusive spectrum of the reaction ^{208}Pb(α,^{3}He)^{209}Pb at $E_{\rm inc}$ = 30 MeV/nucleon [7]. Curve (a) is our total cross section; curve (b) is the breakup multiplied by a factor 10. The other curves are the individual $l_f = 6 - 10$ contributions to the absorption as indicated on the picture. (b) Same as (a). In this case the dotted curves correspond to the calculations made with the semiclassical S matrix. (c) Spectrum of the reaction ^{90}Zr(α,^{3}He)^{91}Zr at $E_{\rm inc}$ = 30 MeV/nucleon [7]. The solid curve superimposed onto the experimental spectrum is our calculation of the inclusive cross section while the solid curve in the lower part of the figure is the calculated breakup. The individual l_f = 3–8 final angular momentum contributions are also shown as indicated in the lower part of the figure. (d) ^{64}Ni(α,^{3}He)^{65}Ni at $E_{\rm inc}$ = 30 MeV/nucleon [7]. The notation is analogous to the previous figure and in this case the bump can be attributed to the population of the l_f = 4–5 final states. (e) Results of the reaction ^{120}Sn(α,^{3}He)^{121}Sn at $E_{\rm inc}$ = 30 MeV/nucleon [7]. The solid curve superimposed to the experimental spectrum is the calculated inclusive cross section. The breakup contribution is indicated by the dotted curve. The l_f = 4–7 contributions are also shown.

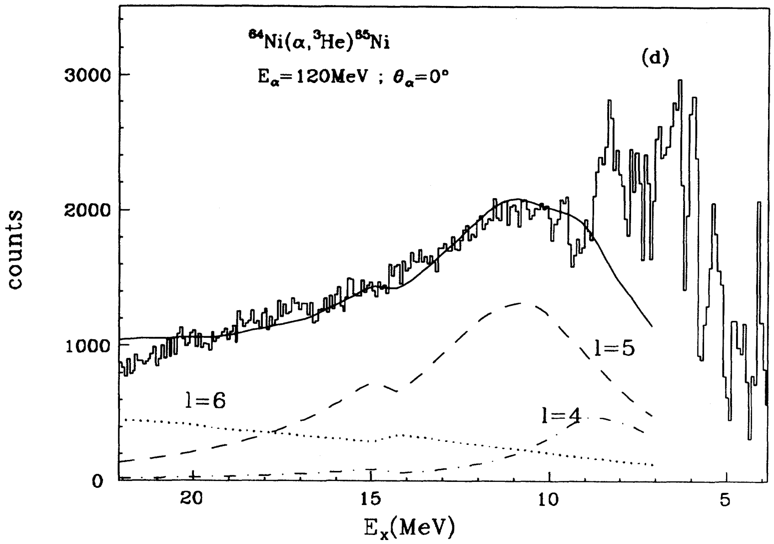

FIG. 3. (*Continued*).

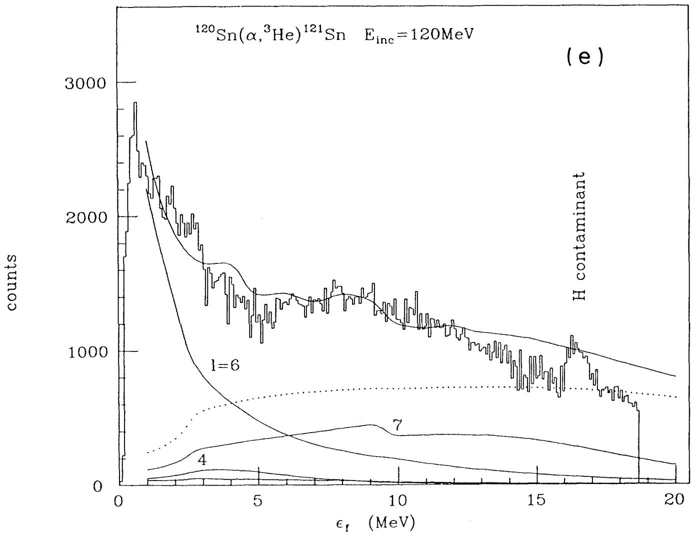

gives a very reasonable estimate of the spreading widths of the single-particle states.

In Fig. 3(c) we show the spectrum of the reaction ^{90}Zr(α,^{3}He)^{91}Zr at $E_{\rm inc}$ = 30 MeV/nucleon [7]. The solid curve superimposed onto the experimental spectrum is our calculation of the inclusive cross section while the solid curve in the lower part of the figure is the calculated breakup. We show also the individual $l_f = 3$–8 final angular momentum contributions from the optical model calculation. One notices that the big bump in the experimental spectrum can be attributed to the combined effects of the $l_f = 5$–6 final angular momenta corresponding to the population of the $1h_{9/2}$ and $1i_{13/2}$ states in ^{91}Zr. The rising of the $l_f = 5$ contribution towards negative final energies is due to the presence of the $1h_{11/2}$ bound state which has a large probability of being populated since in this reaction the spin-matching conditions [27] require $j_i = l_i + 1/2 \to j_f = l_f + 1/2$.

Figure 3(d) refers to the reaction ^{64}Ni(α,^{3}He)^{65}Ni at $E_{\rm inc}$ = 30 MeV/nucleon [7]. The notation is the same as in Fig. 3(c) and in this case the bump can be attributed to the population of the $l_f = 4 - 5$ final states.

Finally in Fig. 3(e) we show the results of the reaction ^{120}Sn(α,^{3}He)^{121}Sn at $E_{\rm inc}$ = 30 MeV/nucleon [7]. In this case the spectrum looks quite different from the previous ones because it contains a large breakup contribution indicated by the dotted curve. There is a peak at about ε_f = 1 MeV due to the $l_f = 6, j_f = 13/2$ single-particle state which is the only one strongly populated. The $l_f = 7$ contribution is spread over all final energies, thus showing that the state $1j_{15/2}$ is completely damped in ^{121}Sn.

We turn now to the discussion of the reactions made at high incident energy.

Figure 4 refers to the reaction ^{207}Pb(^{20}Ne,^{19}Ne)^{208}Pb at $E_{\rm inc}$ = 48 MeV/nucleon. The experimental spectrum

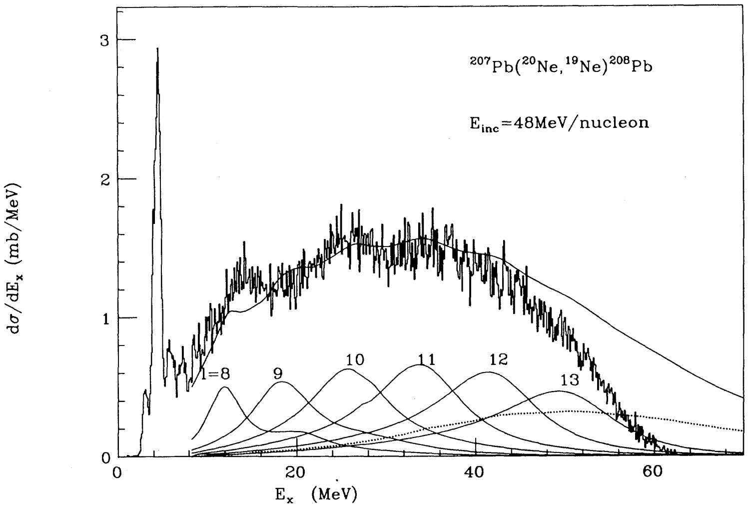

FIG. 4. Inclusive spectrum of the reaction ^{207}Pb(^{20}Ne,^{19}Ne)^{208}Pb at $E_{\text{inc}} = 48$ MeV/nucleon [10]. The solid curve superimposed onto the experimental spectrum is the result of our calculation. The dotted curve shows the calculated breakup while the curves labeled $l_f = 8$–13 show individual contributions to the absorption cross section of several final angular momenta.

is compared to the calculated inclusive cross section. The details of such a calculation were explained in Ref. [10]. The discrepancy between experiment and calculation for energies larger than 50 MeV is due to a cut in the experimental spectrum [10]. In the lower part of the figure we show also the contributions to the cross section of the $l_f = 8 - 13$ terms.

It is interesting to notice that the experimental spectrum has three bumps at $E_x \sim 14$ MeV, $E_x \sim 25$ MeV, and $E_x \sim 34$ MeV. At the same excitation energies also the calculated spectrum has bumps and from the l_f decomposition in the low part of the figure we notice that the bumps correspond to the maximum value of the $l_f = 8$, $l_f = 10$, and $l_f = 11$ contributions. However, because of the cut in the experimental spectrum, it is not so clear that the $l_f = 11$ state gives rise to an isolated bump. The $l_f = 8$ term shows two peaks. The first one corresponds to the $1k_{17/2}$ state, while the second one around $E_x \sim 20$ MeV corresponds to the $1k_{15/2}$ state.

The dotted curve shows the elastic breakup which is calculated from the first term of Eq. (2.1). This is a very small contribution to the total inclusive cross section in the low-energy part of the spectrum and it has a maximum around $E_x = 50$ MeV. Its effect is just to enhance the $l_f = 10$–11 contributions.

To our knowledge this is the first clear example of the persistence of single-particle effects in the excitation energy region $E_x = 20$–40 MeV. This is possible because in this energy range the widths of the l_f resonances are still smaller than the spacing between them. At higher excitation energies this is not true anymore. In fact the $l_f = 12$ contribution has a total width of about 13 MeV while the spacing between the $l_f = 12$ and $l_f = 13$ maxima is about 10 MeV. We remind the reader that the widths of the l_f resonances calculated with the optical model S matrix depend both on the real as well as on the imaginary parts of the optical potential and then they are the sum of the escape plus spreading widths. The optical potential used for this calculation [10] is different from the potential used for the previous reaction on lead [15] shown in Fig. 3(a). The main difference is that for final energies larger that 10 MeV the real potential of Ref. [15] is shallower than ours for about 3 MeV. As a result the peaks of the $l_f = 9$ and $l_f = 10$ terms in Fig. 3(a) are shifted by about 4 MeV with respect to the results shown in Fig. 4 and resumed in Table III, but the peak of the $l_f = 8$ contribution in Fig. 3(a) fits very well the bump in the experimental spectrum.

Then from the analysis of Fig. 4 we can conclude that the transfer to the continuum inclusive spectrum of ^{208}Pb at incident energy $E_{\text{inc}} = 48$ MeV is still dominated by absorption effects on single-particle high-angular-momentum states of the target. This is due to various combined facts. One is that the single-particle damping is not very large for excitation energies lower than 40 MeV and also the escape probability of the particle from the potential pocket via barrier penetration is small. Furthermore, there are good matching conditions between the initial and final energies and angular momenta of the neutron in the projectile and target, respectively, and this enhances the transfer probability.

Figure 5 shows the experimental and calculated spectra of the reaction ^{208}Pb(^{40}Ar,^{39}Ar)^{209}Pb at $E_{\text{inc}} = 41$ MeV/nucleon [6,10]. In Ref. [10] we showed that this reaction is dominated by the transfer from the $1d_{3/2}$ initial state in ^{40}Ar (solid curve superimposed onto the experimental spectrum). The l_f decomposition in the lower part of the figure refers to the transfer cross section from this initial state only. As in the previous reaction the $l_f = 8$ term (solid curve) gives rise to two peaks. The individual $1k_{17/2}$ contribution is shown separately by the dotted curve. The second peak in the solid curve is due to the $1k_{15/2}$ and it is higher that the first one because in this case the spin-matching condition requires

TABLE III. Resonance energies in ^{208}Pb.

l_f	6	7	8	9	10
ε_{res} (MeV)	3.2	4.8	5.5	12	19

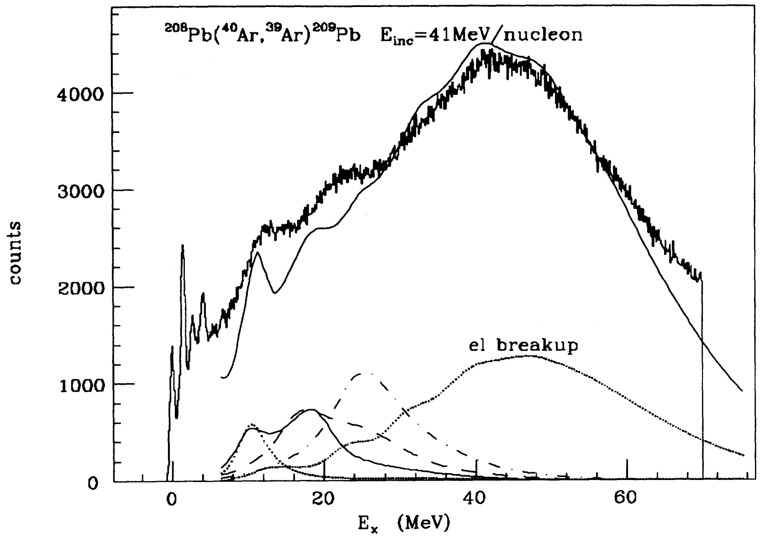

FIG. 5. Inclusive spectrum of the reaction $^{208}\text{Pb}(^{40}\text{Ar},^{39}\text{Ar})^{209}\text{Pb}$ at $E_{\text{inc}} = 41$ MeV/nucleon [10]. The solid curve superimposed onto the experimental spectrum is the result of our calculation for the cross section due to transfer from the $1d_{3/2}$ initial state in Ar. In the lower part of the figure the dotted curve shows the contribution of the $1k_{17/2}$ final state. The solid curve is the total contribution due to $l_f = 8$. The second peak is due to the $1k_{15/2}$ state. The dashed line is the contribution of $l_f = 9$ and the dot-dashed line is for $l_f = 10$. The tightly dotted curve is the elastic breakup.

$j_i = l_i - 1/2 \to j_f = l_f - 1/2$. The $l_f = 9$ (dashed line) contribution has quite a large width and its contribution does not give a definite bump in the experimental spectrum; rather it is responsible together with the $l_f = 10$ contribution shown by the dot-dashed curve, for the second bump in the experimental spectrum. This result confirms the analysis done for the previous reaction, namely, that the experimental spectra contain evidence for the population by transfer of the $l_f = 10$ state in ^{208}Pb and ^{209}Pb.

Figure 6 shows the calculated inclusive spectrum of the reaction $^{90}\text{Zr}(^{20}\text{Ne},^{19}\text{Ne})^{91}\text{Zr}$ at $E_{\text{inc}} = 40$ MeV/nucleon. From the angular momentum decomposition in the lower part of the figure one notices that the first bump is due to the population of the $1i_{13/2}$ and $1h_{9/2}$ states, while the second bump is due to the $1j_{15/2}$ state. The experimental spectrum for this reaction has been measured [3] and it does show two bumps at energies $E_x = 16$ MeV and $E_x = 30$ MeV corresponding to those predicted by our calculations.

Therefore we can conclude that the resonant behavior of the transfer inclusive spectra so far analyzed does correspond in fact to an absorption of the neutron into states of the target which have definite angular momentum and a Lorentzian distribution around the resonance energy. We can predict the widths of these states with good accuracy by using Eqs. (3.1), (3.2), and (3.7). Our analysis predicts the persistence of single-particle effects in lead up to $l_f = 10$ at $E_x \approx 26$ MeV. However, the $l_f = 11$ and $l_f = 12$ states give also a resonant behavior around $E_x \simeq 32$ MeV and $E_x \simeq 42$ MeV, respectively, as shown in Fig. 4, but such energies are very close to the top of their respective potential barriers which are at 30 MeV and 35 MeV. Then the treatment of these states as single-particle potential resonances cannot be justified so well and we conclude that the resonant behavior is due only to an optimum Q-value effect. In ^{91}Zr single-particle states are populated up to $E_x \sim 30$ MeV.

Finally Fig. 7 shows the results of the reaction $^{48}\text{Ca}(^{20}\text{Ne},^{19}\text{Ne})^{49}\text{Ca}$ at $E_{\text{inc}} = 48$ MeV/nucleon [8]. The

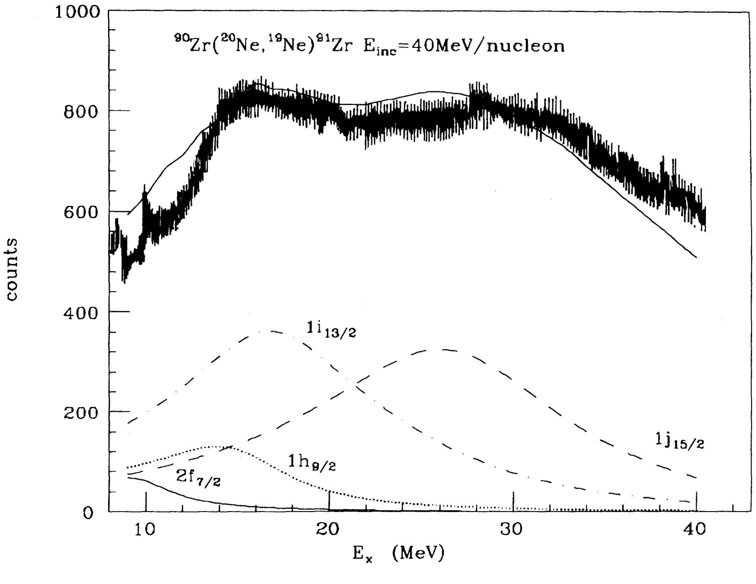

FIG. 6. Calculated inclusive spectrum of the reaction $^{90}\text{Zr}(^{20}\text{Ne},^{19}\text{Ne})^{91}\text{Zr}$ at $E_{\text{inc}} = 40$ MeV/nucleon superimposed onto the experimental spectrum [3]. The final angular momentum decomposition is shown in the lower part of the figure.

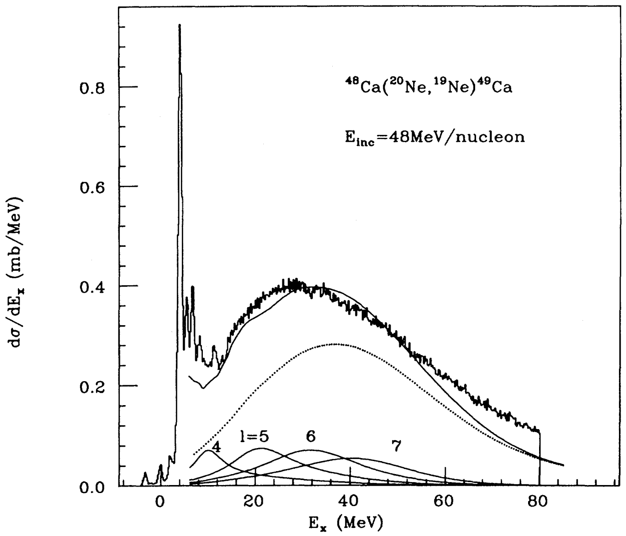

FIG. 7. Results of the reaction ^{48}Ca(^{20}Ne,^{19}Ne)^{49}Ca at $E_{\rm inc}$ = 48 MeV/nucleon [8]. The solid curve superimposed onto the experimental spectrum is the calculated inclusive cross section. The dotted curve is the total breakup. The final angular momentum decomposition is shown in the lower part of the figure.

solid curve superimposed onto the experimental spectrum is the calculated inclusive cross section. The dotted curve is the total breakup which in this case gives the dominant contribution to the spectrum. This result is consistent with the l_f decomposition shown in the lower part of the figure. Only the $l_f = 4$ contribution, centered around $E_x = 9$ MeV seems to have a single-particle behavior. All the other contributions have widths larger than their spacing and we have checked than their resonance energies are higher than the top of the corresponding real plus centrifugal potentials. Then also in this case the resonant behavior of the individual l_f terms does not correspond to the population of a single-particle state but rather to an energy-matching effect. The experimental spectrum does not show any isolated bump, but just a structureless continuum with a maximum corresponding to the maximum breakup probability.

V. CONCLUSIONS

In this paper we have studied the microscopic origin of the resonant structures shown by several one-neutron transfer to the continuum experimental spectra. It has been demonstrated that they are due to the population of single-particle states of positive energy and high angular momentum.

The single-particle nature of the excitations has been clarified by introducing a semiclassical S matrix which describes the rescattering of the neutron on the target. Near resonance the semiclassical S matrix exhibits a Lorentzian shape with an explicit dependence on the width. We have shown that within the semiclassical theory the width can be written as a sum of an escape width plus a spreading width. The physical meaning of these two terms has been discussed and we have given some prescription to calculate them.

The spreading width has been analyzed in great detail because it gives the largest contribution to the total width. Three different ways of calculating it have been proposed and the numerical values obtained agree within 20%. The spreading widths increase smoothly with the neutron energy in the continuum following the energy dependence of the imaginary part of the optical potential. It was also shown that the dependence on the angular momentum is negligible.

Our calculations suggest that the low-energy bump shown by the spectra of the reactions made at $E_{\rm inc} = 30$ MeV/nucleon is due to the population of single-particle states of high angular momentum but low final energy.

On the other hand, the results of our analysis seem to suggest that single-particle effects in lead and zirconium persist at excitation energies as high as 20–30 MeV. The reason is that states like the $1m_{21/2}$ in lead or the $1j_{15/2}$ in zirconium have resonance energies which are still below the top of the barrier formed by the real plus centrifugal plus spin-orbit potentials and their escape probabilities by barrier penetration are small. Furthermore, the strength of the imaginary part of the neutron-^{208}Pb optical potential which depends on the mixing between the single-particle states and other modes of excitation increases up to about $E_x = 40$ MeV where it starts to saturate. As a consequence, the spreading widths below 40 MeV remain smaller than the spacing between the resonances which then can still be considered isolated. Because of these properties, the single-particle resonances are preferred modes of excitation in a transfer reaction to targets like ^{208}Pb and ^{90} Zr.

This point has been illustrated by the analysis of the reactions ^{207}Pb(^{20}Ne,^{19}Ne)^{208}Pb at $E_{\rm inc}$ = 48 MeV/nucleon, ^{208}Pb(^{40}Ar,^{39}Ar)^{209}Pb at $E_{\rm inc}$ = 41 MeV/nucleon [6, 10], and ^{90}Zr(^{20}Ne,^{19}Ne)^{91}Zr at $E_{\rm inc}$ = 40 MeV/nucleon [3]. It has been shown that the $l_f = 10$ final state corresponding to the $1m_{21/2}$ single-particle resonance centered around $\varepsilon_f \sim 20$ MeV in ^{208}Pb can be populated by one-neutron transfer with a probability higher than underlying states and the experimental spectrum shows a bump in correspondence to this state, thus indicating that the single-particle damping is not complete yet. The estimated escape width for this state is about 1 MeV which is the same order of magnitude as the spreading width and one could hope to detect a noticeable direct decay of this state by performing an experiment similar to the one of [7]. A similar result holds for the $1j_{15/2}$ state in ^{91}Zr at $\varepsilon_f \sim 18$ MeV.

The fact that at $E_{\rm inc}$ =40–50 MeV/nucleon transfer reactions on heavy targets dominate the inclusive cross section suggests that the description of the nucleus by a mean field is still valid. This remark might be useful for the understanding of the fragmentation process which is the dominant reaction mechanism at higher incident energies.

All the above remarks hold true because, in the reactions we have described, the background due to breakup is small. This is due to the fact that the initial bound state energy of the neutron in the projectile is large, of the order of 10–20 MeV, and the incident energy per nucleon is of the same order of magnitude such that the energy-matching condition gives a most favorite final energy which is in the range of persistence of single-particle states. In the case of the reactions on ^{120}Sn and ^{48}Ca instead, the most favorite final energies do not correspond to any single-particle resonance state of the targets and the spectra are dominated by the breakup.

The results would again be different for a reaction having a projectile with a loosely bound neutron like ^{11}Be or if the incident energy were much higher [12]. In those cases also the inclusive spectra would be dominated by the direct breakup component.

ACKNOWLEDGMENTS

It is my pleasure to thank David Brink for numerous enlightening discussions on the semiclassical S matrix and Sydney Galès, Simone Fortier, Nimet Frascaria, and their groups for a long correspondence and for allowing me to use several unpublished experimental spectra. Also I would like to mention the kindness of Claude Mahaux in providing me with the numerical values of some optical potential strengths and of Massimo Di Toro for reading an early version of this paper.

APPENDIX A

In this appendix we derive Eq. (3.1) given in Sec. III A.

First we give the definitions of S_{32} and A which appear in Eq. (2.6),

$$\exp(2iS_{32}) = A\exp(2i\psi). \tag{A1}$$

S_{32} is a WKB integral defined as

$$S_{32} = \int_a^b |\gamma(r)|dr, \tag{A2}$$

where

$$\gamma^2(r) = \left|\frac{2m}{\hbar^2}[V(r) + iW(r) - \varepsilon_{\rm res}] + \frac{l(l+1)}{r^2}\right| . \tag{A3}$$

In Eq. (A2) a and b are the inner and outer turning points which appear when the real potential has three turning points. Also

$$A = \exp(2{\rm Im}S_{32}) = \exp\left(\frac{2}{\hbar}\int_a^b W(r(t))dt\right), \tag{A4}$$

where $W(r(t))$ is the imaginary part of the potential which appears in Eq. (A3).

If the imaginary part of the potential is small, one can expand the exponential in the above definition of A and then get

$$A \approx 1 + 2\bar{W} \tag{A5}$$

and

$$A^{-1/2} = 1 - \bar{W}, \tag{A6}$$

where

$$\bar{W} = \frac{1}{\hbar}\int_a^b W(r(t))dt. \tag{A7}$$

The step between Eq. (2.7) and Eq. (2.8) is made by expanding about the resonance position $\cos(2\psi) \approx -1 + \alpha(\varepsilon_f - \varepsilon_{\rm res})^2$. The expansion coefficient α is given by

$$\alpha = 2\left(\frac{\partial S_{32}}{\partial\varepsilon_f}\right)^2 |_{\varepsilon_f=\varepsilon_{\rm res}} = 2\left(\frac{\tau}{\hbar}\right)^2, \tag{A8}$$

where τ is half the period of the classical orbit inside the real potential pocket defined by Eq. (3.4).

Then Eq. (2.8) is obtained from Eq. (2.7) if one defines a width Γ as

$$\Gamma = \sqrt{2}\left(\frac{1 - A\sqrt{1-P}}{\sqrt{A\alpha\sqrt{1-P}}}\right), \tag{A9}$$

where P is the barrier penetration factor defined in Sec. II.

Now, since $P < 1$, we can expand $\sqrt{1-P}$ and use also the approximated forms of A and $\sqrt{A}$ given above which are valid when the imaginary potential is small. Then we get for Γ

$$\begin{aligned}\Gamma &= \sqrt{\frac{2}{\alpha}}\frac{1 - A + \frac{AP}{2}}{\sqrt{A}} \\ &= \sqrt{\frac{2}{\alpha}}\left(\frac{P}{2} - 2\bar{W} + P\bar{W}\right)(1-\bar{W}) \\ &\approx \sqrt{\frac{2}{\alpha}}\left(-2\bar{W} + \frac{P}{2}\right) \\ &= \frac{\hbar P}{T} - 2\frac{\hbar}{\tau}\bar{W} = \Gamma_0 + 2\langle W\rangle. \end{aligned}\tag{A10}$$

In getting the above result we neglected terms of the order $P\bar{W}$ and we defined also $\Gamma_0 = \hbar P/T$ [cf. Eq. (3.2)]. Finally we defined the time average of the imaginary potential as

$$\langle W\rangle = -\frac{\int_a^b W(r(t))dt}{\tau} . \tag{A11}$$

The minus sign in the above equation is correct since in this paper we use a negative strength for the imaginary potential.

APPENDIX B

In this appendix we show the equivalence between Eq. (3.5) and Eq. (3.6). We start from

$$\Gamma^{\downarrow} = -2\int\rho(r)W(r)\, d^3r, \tag{B1}$$

where $\rho(r)$ is the single-particle density given by $\rho(r) = |\psi(r)|^2$ and $\psi(r)$ is the single-particle wave function which depends on the quantum numbers l and m as well as on the single-particle energy. In the following we omit those indices for brevity. Let

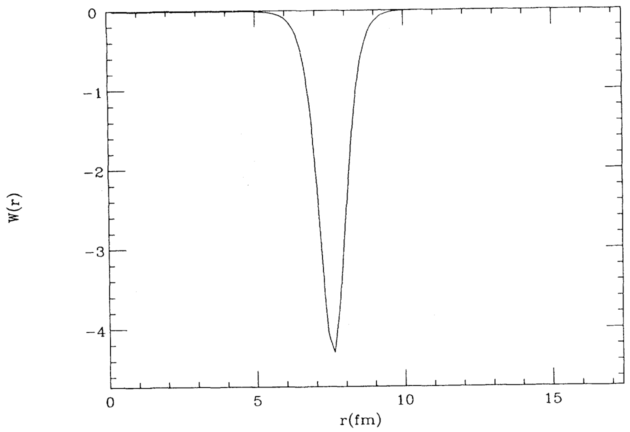

FIG. 8. Radial dependence of the imaginary part of the optical potential for ^{208}Pb with the strength appropriate to $\varepsilon_f = 6.8$ MeV.

$$|\psi(\mathbf{r})|^2 = \left|\frac{\phi(r)}{r} Y_{lm}(\Omega)\right|^2 \tag{B2}$$

and let us take for the radial wave function $\phi(r)$ its semiclassical form

$$\phi(r) = \frac{C}{\sqrt{\gamma}} \sin\left(\text{Re } S_{32} + \frac{\pi}{4}\right), \tag{B3}$$

where S_{32} is the WKB integral defined in Appendix A and the normalization constant C is defined in terms of the classical period as

$$|C|^2 = \frac{2m}{\hbar}\frac{1}{\tau}. \tag{B4}$$

Then we insert these values into Eq. (B1) and take out of the integral a factor 1/2 which is the average value of the sine function. Next we perform the angular integration which gives 1. We approximate also the local momentum $\gamma \sim mv/\hbar$ where v is the average velocity inside the potential pocket; in this way we can change the variable of integration from dr to $dt = dr/v$ and we finally obtain

$$\Gamma^{\downarrow} = -2\frac{\int_a^b W(r(t))dt}{\tau}. \tag{B5}$$

APPENDIX C

We discuss now under which conditions it is justified to approximate Eq. (B1) by taking a constant value for the density of orbitals $\rho(r) \sim \tilde{\rho}$ outside the integral. In Fig. 8 we show the radial dependence of the imaginary part of the optical potential used for ^{208}Pb which according to Ref. [25] is a sum of a volume and a surface term with the energy-dependent strengths calculated at $\varepsilon_f = 6.8$ MeV. Figure 9 shows instead $R(r) = |\phi(r)/r|^2$ for three resonance states in ^{208}Pb, the $2h_{11/2}$, $1k_{17/2}$, and $1j_{13/2}$. $R(r)$ is the modulus square of the radial part of the wave function, Eq. (B2), normalized such that $\int |\phi(r)|^2 dr = 1$. One notices that while the $2h_{11/2}$ state has a node and it has its main peak inside the nuclear surface, the $1k_{17/2}$ and $1j_{13/2}$ states are instead peaked at the surface where also the imaginary potential gives its main contribution. In this case the radius of the nucleus is $R = 7.2$ fm. Therefore it seems reasonable to take the density of

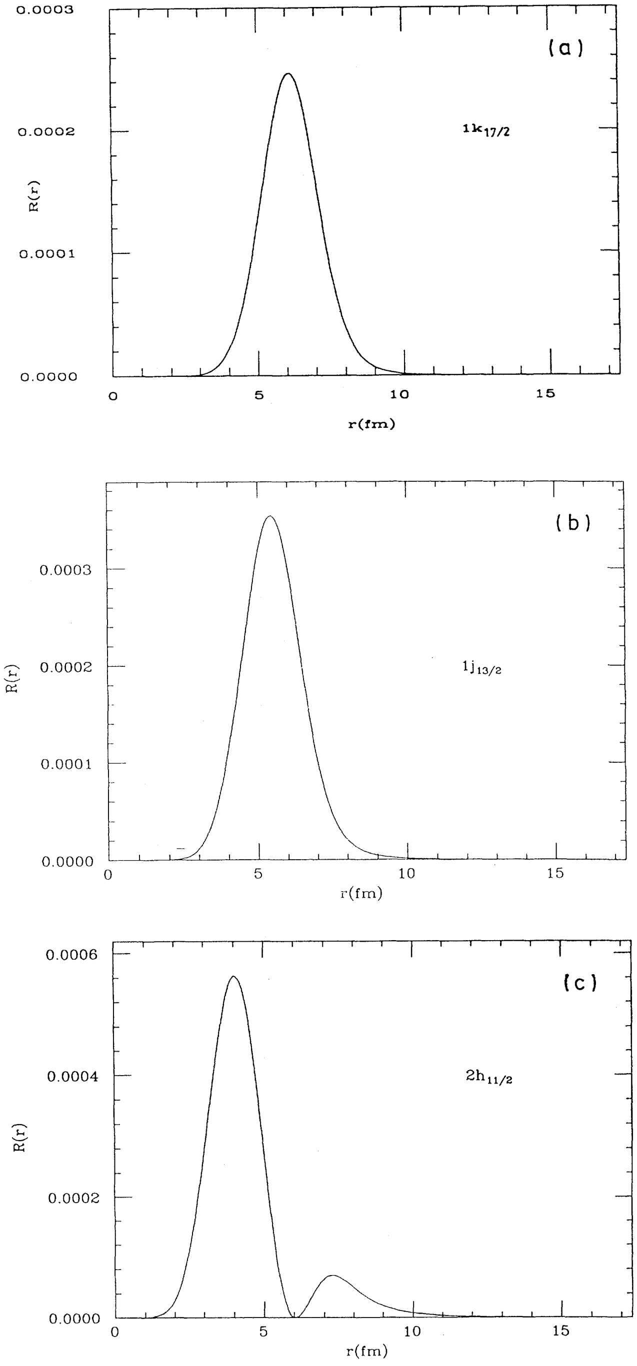

FIG. 9. $R(r) = |\phi(r)/r|^2$ for three resonance states in ^{208}Pb, the (a) $1k_{17/2}$, (b) $1j_{13/2}$, and (c) $2h_{11/2}$. $R(r)$ is the modulus square of the radial part of the wave function, Eq. (B2).

TABLE IV. Spreading widths from Eq. (3.6) with the exact wave functions.

Nucleus	l_f	ε_{res} (MeV)	$\Gamma^{\downarrow}$ (MeV)
^{208}Pb	5	4.02	1.90
	7	6.82	2.01
	8	6.22	3.12
^{91}Zr	6	8.62	10.17
	7	17.8	11.14

orbitals to be constant outside the integral when we are in a region of continuum energies where the shell model predicts only states of high angular momentum whose wave functions have no nodes and are peaked at the nuclear surface. For the three states discussed here we calculated the spreading widths from Eq. (B1) with the exact wave functions shown in Fig. 9 and the resulting values are shown in Table IV. They are smaller by about a factor of 1.85 than the values given in Table II in the case of ^{208}Pb. In Table IV we give also some values of $\Gamma^{\downarrow}$ calculated for ^{91}Zr. In this case the agreement with the values obtained from Eq. (3.7) is very good.

Unfortunately it is rather difficult to get convergence in the numerical solution of the Schrödinger equation for states of angular momentum higher than those discussed here; otherwise one could always calculate Eq. (B1) exactly. Then we suggest that if one is interested only in an estimate of the spreading widths having in mind that their most important characteristic is the energy dependence, Eq. (3.7) can be used together with an appropriate density of orbitals and with a good parametrization of the volume integral of the imaginary part of the optical potential.

Finally we notice that the value of the resonance energies are different than those given in Table III; this is because the values given here come from the solution of the Schrödinger equation while those of Table III correspond to the peaks of the l resonant terms of the transfer probability Eq. (2.1).

[1] S. Galès, Ch. Stoyanov, and A.I. Vdovin, Phys. Rep. **166**, 125 (1988), and references therein.

[2] S. Fortier, S. Gàles, S.M. Austin, W. Benenson, G.M. Crawley, C. Djalali, J.S. Winfield, and G. Yoo, Phys. Rev. C **41**, 2689 (1990).

[3] D. Beaumel, Y. Blumenfeld, Ph. Chomaz, N. Frascaria, J.P. Garron, J.C. Roynette, T. Suomijärvi, J. Barrette, B. Berthier, B. Fernandez, J. Gastebois, and W. Mittig, 1987, Annual Report IPN-Orsay, p. 41.

[4] C.P. Massolo, S. Fortier, S. Galès, F. Azaiez, E. Gerlic, J. Guillot, H. Hourani, H. Langevin-Joliot, J.M. Maison, J.P. Shapira, and G.M. Crawley, Phys. Rev. C **43**, 1687 (1991).

[5] G.H. Yoo, G.M. Crawley, N.A. Orr, J.S. Winfield, J.E. Finck, S. Galès, Ph. Chomaz, I. Lhenry, and T. Suomijärvi, Phys. Rev. C **47**, 1200 (1993).

[6] I. Lhenry. Ph.D. thesis, Report No. IPNO-T92-01, IPN, Orsay, 1992; I. Lhenry, T. Suomijärvi, Y. Blumenfeld, Ph. Chomaz, N. Frascaria, J.P. Garron, J.C. Roynette, J.A. Scarpaci, D. Beaumel, S. Fortier, S. Gàles, H. Laurent, A. Gillibert, G. Crawley, J. Finck, G. Yoo, and J. Barreto (unpublished).

[7] D. Beaumel, S. Fortier, S. Galès, J. Guillot, H. Langevin-Joliot, H. Laurent, J.M. Maison, J. Vernotte, J. Bordewijck, S. Brandenburg, A. Krasznahorkay, G.M. Crawley, C.P. Massolo, and M. Renteria, Phys. Rev. C **49**, 2444 (1994).

[8] H. Laurent, D. Beaumel, S. Fortier, S. Galès, I. Lhenry, J.M. Maison, Y. Blumenfeld, N. Frascaria, J. Guillot, J.C. Roynette, J.A. Scarpaci, T. Suomijärvi, and A. Gillibert, in *Contributed Papers to The N-N Collisions V Conference,* Taormina, Italy, 1994, edited by M. Di Toro, P. Piattelli, and P. Sapienza (INFN-LNS, Catania, 1994), p. 31.

[9] I. Lhenry, T. Süomijarvi, Ph. Chomaz, and N. van Giai, Nucl. Phys. **A565**, 524 (1993).

[10] A. Bonaccorso, I. Lhenry, and T. Suomijärvi, Phys. Rev. C **49**, 329 (1994).

[11] A. Bonaccorso and D.M. Brink, Phys. Rev. C **38**, 1776 (1988).

[12] A. Bonaccorso and D.M. Brink, Phys. Rev. C **43**, 299 (1991).

[13] A. Bonaccorso and D.M. Brink, Phys. Rev. C **44**, 1559 (1991).

[14] A. Bonaccorso and D.M. Brink, Phys. Rev. C **46**, 700 (1992).

[15] C. Mahaux and R. Sartor, Adv. Nucl.Phys. **20**, 1 (1991).

[16] D.M. Brink and N. Takigawa, Nucl. Phys. **A309**, 159 (1977).

[17] D.M. Brink, *Semiclassical Methods in Nucleus-Nucleus Scattering* (Cambridge University Press, Cambridge, England, 1985), p. 97; private communication.

[18] A. Bohr and B.R. Mottelson, *Nuclear Structure* (Benjamin, New York, 1969), Vol. 1, p. 446.

[19] L.D. Landau and E.M. Lifshitz, *Quantum Mechanics* (Pergamon, London, 1958), Chap. VII.

[20] N. Van Giai and Ch. Stoyanov, Phys. Lett. B **272**, 178 (1991).

[21] J. Bang, F.A. Gareev, I.V. Puzynin, and R.M. Jamalejev, Nucl. Phys. **A261**, 59 (1976).

[22] Computer code MATHEMATICA, Stephen Wolfram (Addison-Wesley, Redwood City, CA, 1988).

[23] G. Bertsch, P. Bortignon, and R. Broglia, Rev. Mod. Phys. **55**, 289 (1983).

[24] G.E. Brown and M. Rho, Nucl. Phys. **A372**, 397 (1981).

[25] C. Mahaux and R. Sartor, Nucl. Phys. **A493**, 157 (1989).

[26] C. Mahaux and R. Sartor, Nucl. Phys. **A568**, 1 (1994) .

[27] A. Bonaccorso, D.M. Brink, and L. Lo Monaco, J. Phys. G **13**, 1407 (1987).